

# Viewing Black Holes by Waves

Ken-ichiro Kanai\* and Yasusada Nambu†

*Department of Physics, Graduate School of Science,  
Nagoya University, Chikusa, Nagoya 464-8602, Japan*

(Dated: June 15, 2013, ver. 0.99)

## Abstract

We study scattering of waves by black holes. Solving a massless scalar field with a point source in the Schwarzschild spacetime, waves scattered by the black hole is obtained numerically. We then reconstruct images of the black hole from scattered wave data for specified scattering angles. For the forward and the backward directions, obtained wave optical images of black holes show rings that correspond to the black hole glories associated with existence of the unstable circular photon orbit in the Schwarzschild spacetime.

PACS numbers: 04.20.-q, 42.25.Fx

Keywords: wave optics; image formation; black hole; wave scattering

arXiv:1303.5520v2 [gr-qc] 19 Jul 2013

---

\*Electronic address: kanai@gravity.phys.nagoya-u.ac.jp

†Electronic address: nambu@gravity.phys.nagoya-u.ac.jp

## I. INTRODUCTION

Wave scattering and resulting diffraction effect are related to familiar phenomena such as rainbows and glories. These phenomena are caused by scattering of light by water droplet in atmosphere and analysis based on the wave optics is required to understand its formation and quantitative nature [1]. The methodology and the formalism of the wave scattering problem are applied to wide fields in physics for the purpose of obtaining the information of the scatterer by analyzing the date of the scattering wave. For the gravitational physics, the wave related properties of black hole spacetimes have been investigated by many researchers for more than 40 years to obtain physical nature of black holes [2–9]. T. Regge and J. A. Wheeler [2] investigated the wave equation for gravitational perturbations in black hole spacetimes and have shown that the Schwarzschild black hole is stable against the perturbations. For the spinning Kerr black hole, it was shown that the incident wave is amplified if the wave satisfies an appropriate condition. This phenomena is called super radiance and peculiar to the Kerr spacetime accompanying with the dragging effect [10]. The quasi-normal oscillation of black holes is also wave related property and this normal mode is characterized by parameters of black holes [10]. As a straightforward application of the wave scattering theory, cross sections of black holes are obtained from the scattering waves and the nature of the black hole geometry is discussed from the view point of waves. Especially, peculiar to the wave scattering by the black hole, the diffraction effect for the backward scattered wave becomes significant and this leads to the phenomena so called the black hole glories [3, 5]. The main purpose of the wave scattering problem by black holes is theoretical understanding of the physics of black holes and wave propagation in curved spacetimes. For astrophysical black holes, it is unlikely that wave effects such as diffraction can be observed using current technology, but there is a possibility that future technology enable us to study interference effects in gravitationally lensed waves.

The treatment of the conventional wave scattering by black holes mainly concerns analysis of the scattering amplitude and the cross section. In this paper, we consider wave scattering by black holes from the view point of image formation. Our main motivation is to investigate “images” of black holes formed by the incident wave using wave optics [11, 12]. In the geometric optics, “images” of black holes are obtained by solving null geodesics (light rays) in black hole spacetimes and we can draw images of a black hole as “black hole shadows”; if we assume a light source behind a black hole is larger than the angular size of the black hole, a distant observer see a dark spot that corresponds to the apparent image of the black hole. We expect to obtain the shadow image of the black hole in the framework of wave scattering problems. However, obtaining images using waves is not trivial task at first sight; as is known, the scattering amplitude at the observer shows diffraction pattern due to interference between scattered waves. However, this diffraction pattern is not itself images of the black hole. The theory of image formation in wave optics tells that we must decode scattered waves using imaging device to reconstruct images [13]. The scattered waves by a black hole contains information of the black hole geometry and it is possible to reconstruct images of the black hole. For this purpose, we introduce a convex lens to the configuration of the standard wave scattering by black holes and aim to reconstruct images from scattering waves.

In this paper, we consider scattering of massless scalar waves by a Schwarzschild black hole. The massless scalar waves are adopted as the benchmark treatment for wave scattering problems by black holes and we do not consider polarization degrees of freedom that is

necessary for the electro magnetic waves and gravitational waves. We investigate images of the black hole using wave optics. As the source of incident waves, we prepare a point source of the wave placed near the black hole. This models the astrophysical black holes with active emission regions such as accretion disks around them. We solve the wave equation for the massless scalar field (Helmholtz equation) using the finite difference method. Then, we reconstruct images from scattering wave data and investigate characteristics of the black hole spacetime appearing in images. This paper is organized as follows. In Sec. II, we introduce basic equations and our numerical method for solving the scalar wave equation. In Sec. III, we explain the method of images reconstruction from scattering waves. In Sec. IV, we present our numerical results and Sec. V is devoted to summary. We use units in which  $c = \hbar = G = 1$  throughout this paper.

## II. WAVE SCATTERING IN BLACK HOLE SPACETIMES

We solve the wave equation for the massless scalar field in the Schwarzschild spacetime numerically. For this purpose, we rewrite the Klein-Gordon equation for the scalar field to the Helmholtz equation assuming that the wave field is monochromatic. Then by finite differentiating the equation, we obtain the numerical solution of the wave scattering problem. The detail of the finite difference method to solve the wave equation is presented in Appendix.

### A. Scalar wave equation in Schwarzschild spacetime

For the massless scalar field  $\Phi$ , the scalar wave equation in a curved spacetime is

$$\square\Phi = \frac{1}{\sqrt{-g}}\partial_\mu(\sqrt{-g}g^{\mu\nu}\partial_\nu\Phi) = S, \quad (1)$$

where  $S$  is a source term of the wave. For the Schwarzschild spacetime, the metric is

$$ds^2 = -\left(1 - \frac{2M}{r}\right) dt^2 + \left(1 - \frac{2M}{r}\right)^{-1} dr^2 + r^2(d\theta^2 + \sin^2\theta d\phi^2), \quad (2)$$

and the wave equation in the Schwarzschild spacetime is

$$\begin{aligned} & -\left(1 - \frac{2M}{r}\right)^{-1} \frac{\partial^2\Phi}{\partial t^2} + \frac{1}{r^2} \frac{\partial}{\partial r} \left[ r^2 \left(1 - \frac{2M}{r}\right) \frac{\partial\Phi}{\partial r} \right] \\ & + \frac{1}{r^2} \left[ \frac{1}{\sin\theta} \frac{\partial}{\partial\theta} \left( \sin\theta \frac{\partial\Phi}{\partial\theta} \right) + \frac{1}{\sin^2\theta} \frac{\partial^2\Phi}{\partial\phi^2} \right] = S(t, r, \theta, \phi). \end{aligned} \quad (3)$$

We consider the solution of this equation corresponding to the wave scattering problem by the black hole; the wave is emitted by a point source placed at  $r = r_s, \theta = \pi$  (on the  $\bar{z}$  axis) and scattered by the black hole. The scattered wave is observed by a detector placed at  $r = r_{\text{obs}}$  (Fig. 1). We do not consider the motion of the source in this paper. The location of the observer is not restricted on the  $\bar{z}$  axis. We assume that the wave is monochromatic with the angular frequency  $\omega$ . This angular frequency is defined with respect to the Schwarzschild coordinate time  $t$ .

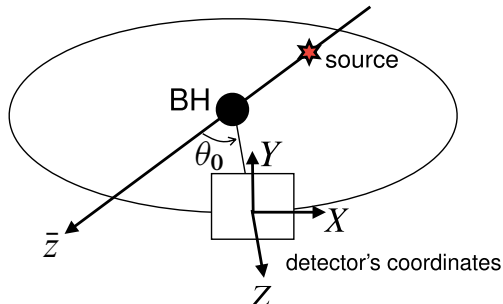


FIG. 1: Configuration of the wave scattering problem by a black hole. We introduce spatial coordinates  $(\bar{x}, \bar{y}, \bar{z}) = (r \sin \theta \sin \phi, r \sin \theta \cos \phi, r \cos \theta)$ . A point source is placed at  $(\bar{x}, \bar{y}, \bar{z}) = (0, 0, -r_S)$ . The scattered waves are observed by a detector at  $(\bar{x}, \bar{y}, \bar{z}) = (r_{\text{obs}} \sin \theta_0, 0, r_{\text{obs}} \cos \theta_0)$ , where  $\theta_0$  corresponds to the scattering angle.

Because the Schwarzschild geometry is spherically symmetric, the source and the black hole system of our scattering problem has an axial symmetry. Thus we can impose the axial symmetry for the wave configuration:  $\partial_\phi \Phi = 0, \partial_\phi S = 0$ . As we assume that the time dependence of the scalar wave is  $\Phi \propto e^{-i\omega t}$ , the wave equation can be written as the following Helmholtz equation:

$$\frac{\partial^2 \hat{\Phi}}{\partial x^2} + \frac{1}{r^2} \left(1 - \frac{2M}{r}\right) \frac{1}{\sin \theta} \frac{\partial}{\partial \theta} \left(\sin \theta \frac{\partial \hat{\Phi}}{\partial \theta}\right) + \left[\omega^2 - \frac{2M}{r^3} \left(1 - \frac{2M}{r}\right)\right] \hat{\Phi} = S(r - r_S, \theta - \pi) \quad (4)$$

where  $\hat{\Phi} = r\Phi$  and the tortoise coordinate is introduced by  $x = r + 2M \ln(r/2M - 1)$ .  $S(r - r_S, \theta - \pi)$  represents the point source at  $r = r_S, \theta = \pi$ . In terms of the delta functions,

$$S(r - r_S, \theta - \pi) = \frac{1}{r} \left(1 - \frac{2M}{r}\right) \delta(r - r_S) \delta(\cos \theta + 1). \quad (5)$$

## B. Boundary conditions

We must impose boundary conditions to obtain solutions of our wave equation. We first consider the boundary conditions at  $r = 2M$  and  $r = \infty$ . By the definition of black holes, the wave is purely ingoing at the horizon  $r = 2M$ . Near the horizon, the Helmholtz equation becomes

$$\partial_x^2 \hat{\Phi} + \omega^2 \hat{\Phi} = 0. \quad (6)$$

This equation contains the derivative with respect to the radial coordinate only, and the wave propagates perpendicular to the horizon. Taking into account the purely ingoing condition at the horizon, the wave goes through the horizon perpendicular to it. By restoring the time dependence, this boundary condition can be expressed as

$$\left(\partial_x \hat{\Phi} - \partial_t \hat{\Phi}\right) \Big|_{x \rightarrow -\infty} = 0. \quad (7)$$

On the other hand, the wave is purely outgoing at the spatial infinity because the source of wave is located at the finite distance from the black hole and no wave is coming from outside



of the numerical box. Thus we can assume the wave behaves approximately as a spherical wave at the outer boundary. This boundary condition can be expressed as

$$\left(\partial_x \hat{\Phi} + \partial_t \hat{\Phi}\right)\Big|_{x=x_{\text{outer}}} = 0. \quad (8)$$

Of course, this boundary condition is not exact one and this approximated condition works well only for sufficiently large numerical box compared to the size of the black hole and the location of the point source. In our numerical calculation,  $r_{\text{outer}} = 20.5M$  and  $r_S \leq 6M$ . Although Eq. (8) provide an approximated boundary condition, we think it is sufficient for our purpose in this paper.

Next, we consider the boundary condition associated with the symmetry of the system. According to the axial symmetry of the scalar field configuration,  $\hat{\Phi}$  should be an even function with respect to the angle variable  $\theta$ :  $\hat{\Phi}(\theta) = \hat{\Phi}(-\theta)$ ,  $0 \leq \theta \leq \pi$ . Hence, the boundary condition for the wave on  $\bar{z}$  axis is

$$\left.\frac{\partial \hat{\Phi}}{\partial \theta}\right|_{\theta=0,\pi} = 0. \quad (9)$$

In Eq. (4), the first order derivative term  $\cot \theta \partial_\theta \hat{\Phi}$  is contained and its coefficient diverges at  $\theta = 0, \pi$ . Around  $\theta = 0$ , considering the boundary condition (9),

$$\cot \theta \approx \frac{1}{\theta} + O(\theta), \quad \hat{\Phi}'(\theta) \approx \hat{\Phi}''(0)\theta + O(\theta^2) \quad (10)$$

where  $'$  represents the derivative with respect to  $\theta$ . Hence,

$$\cot \theta \hat{\Phi}'(\theta) \approx \hat{\Phi}''(0) + O(\theta) \quad (11)$$

and this term is regular at  $\theta = 0$ . In the similar manner, we can see that the equation (4) is regular at  $\theta = \pi$ . After all, at  $\theta = 0, \pi$ , Eq. (4) reduces to

$$\partial_x^2 \hat{\Phi} + \frac{2}{r^2} \left(1 - \frac{2M}{r}\right) \partial_\theta^2 \hat{\Phi} + \left[\omega^2 - \frac{2M}{r^3} \left(1 - \frac{2M}{r}\right)\right] \hat{\Phi} = S(r - r_S, \theta - \pi). \quad (12)$$

We adopt this equation as the equation to determine the wave field on the  $\bar{z}$  axis ( $\theta = 0, \pi$ ).

Finally, we consider the boundary condition around the point source. Let us consider a location P near the point source S. In the neighborhood of the point source, the asymptotic form of the wave function in the lowest order of the WKB approximation is given by

$$\Phi_P = \frac{\hat{\Phi}_P}{r_P} \sim \frac{A}{\ell_{\text{PS}}} \exp\left(\frac{i\omega \ell_{\text{PS}}}{\sqrt{1 - 2M/r_P}}\right) \quad (13)$$

where  $A$  is a constant representing the strength of the source and  $\ell_{\text{PS}}$  is the spatial proper distance between P and S:

$$\ell_{\text{PS}}^2 \approx \left(1 - \frac{2M}{r_P}\right)^{-1} (r_P - r_S)^2 + r_P^2 (\theta_P - \theta_S)^2 \approx \left(1 - \frac{2M}{r_P}\right) (x_P - x_S)^2 + r_P^2 (\theta_P - \theta_S)^2. \quad (14)$$

We use this asymptotic behavior of the wave to determine the wave field around the point source.

### III. IMAGE FORMATION IN WAVE OPTICS

Most of previous works on wave scattering by black holes aim to obtain the scattering amplitude or the differential cross section to investigate wave effects. On the other hand, we want to consider images constructed from the scattered waves by black holes. By using images, it is also possible to discuss the semi-classical nature of the wave scattering by black holes. We have introduced the method to reconstruct images from waves in the gravitational lensing system [11, 12] and obtained images of gravitational lensing in wave optics. We apply the same method to the wave scattering by black holes. In the wave optics, the image formation can be understood as diffraction effect of waves. For this purpose, image formation devices such as a convex lens are introduced.

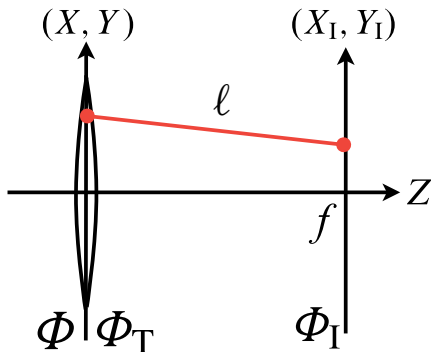


FIG. 2: An image formation system with a convex lens. Incident waves are transformed by the lens and an image of a source object appears on the image plane. This image corresponds to the Fourier transformation of the incident wave.

In our analysis, we adopt a thin convex lens. In this paper, we use a word “lens” to represent a device taking the Fourier transformation of the wave field and “lens” does not necessarily suggest a physical artefact used in optics. Antennas of a VLBI telescope is also a kind of “lens”. Let us  $\Phi(\vec{X})$  be the incident wave in front of the lens and  $\Phi_T(\vec{X})$  is the transmitted wave by the lens.  $\vec{X} = (X, Y)$  denotes the location of a point on the lens plane  $Z = 0$ . These two wave functions are connected by the following relation

$$\Phi_T(\vec{X}) = e^{-i\omega \frac{|\vec{X}|^2}{2f}} \Phi(\vec{X}), \quad (15)$$

where  $f$  represents the focal length of the lens. For a point source placed at  $Z = -f$  (front focal plane), the wave in front of the lens is

$$\Phi(\vec{X}) = e^{i\omega \sqrt{|\vec{X}|^2 + f^2}} \approx e^{i\omega(f + \frac{|\vec{X}|^2}{2f})},$$

where we assumed  $|\vec{X}| \ll f$ . Hence the transmitted wave becomes

$$\Phi_T(\vec{X}) = e^{i\omega f}$$

and its phase becomes independent of  $(X, Y)$ . This means that the transmitted wave is the plane wave. Thus the convex lens converts a spherical wave front to a plane wave front. Now we consider the wave amplitude on the focal plane  $Z = f$  (image plane). Using

the Fresnel-Kirchoff diffraction formula [13], the wave on the image plane is given by the following diffraction integral:

$$\Phi_{\text{I}}(\vec{X}_{\text{I}}) \propto \int_{|\vec{X}| \leq d} d^2 \vec{X} \Phi(\vec{X}) e^{-i\omega \frac{|\vec{X}_{\text{I}}|^2}{2f}} \times \frac{e^{i\omega \ell}}{\ell} \quad (16)$$

where  $\ell$  is path length between a point on the lens plane and a point on the image plane (see Fig. 2) and  $d$  is a radius of the lens. Using  $\ell = \sqrt{|\vec{X} - \vec{X}_{\text{I}}|^2 + f^2} \approx f + |\vec{X} - \vec{X}_{\text{I}}|^2/2f$ ,

$$\Phi_{\text{I}}(\vec{X}_{\text{I}}) \propto \int_{|\vec{X}| \leq d} d\vec{X} \Phi(\vec{X}) e^{-\frac{i\omega}{f}(\vec{X}_{\text{I}} \cdot \vec{X})}. \quad (17)$$

Hence  $\Phi_{\text{I}}$  is the Fourier transformation of the incident wave  $\Phi$ .

Let us consider the situation that the incident wave can be written as the WKB form

$$\Phi(\vec{X}) = A e^{i\omega S(\vec{X})} = A \exp \left[ i\omega \left( S(\vec{X}_*) + \frac{1}{2} S''(\vec{X}_*)(\vec{X} - \vec{X}_*)^2 + \dots \right) \right] \quad (18)$$

where  $\vec{X}_* = (X_*, Y_*)$  denotes the location of the point that the null geodesics intersects with  $Z = 0$  plane. This point corresponds to the classical path of the null ray obtained as the saddle point of the action  $S$ ,  $S'(\vec{X}_*) = 0$ . The classical path is a null geodesics connecting a source and a point on the lens plane. For this form of waves, the wave amplitude on the image plane (17) becomes

$$\begin{aligned} \Phi_{\text{I}}(\vec{X}_{\text{I}}) &\propto \int_{|\vec{X}| \leq d} d^2 \vec{X} \exp \left[ i\omega \left\{ \frac{S''}{2} (\vec{X} - \vec{X}_*)^2 - \frac{\vec{X}_{\text{I}} \cdot \vec{X}}{f} \right\} \right] \\ &\propto \frac{J_1 \left( \omega d \left| S'' \vec{X}_* + \vec{X}_{\text{I}}/f \right| \right)}{\omega d \left| S'' \vec{X}_* + \vec{X}_{\text{I}}/f \right|}. \end{aligned} \quad (19)$$

We have assumed  $|\omega S'' d^2| \ll 2\pi$  and omitted the quadratic term  $|\vec{X}|^2$  in the exponent to evaluate the integral at the last step of the calculation; this is the condition for the Fraunhofer diffraction. On the dimensional analysis,  $S'' \sim 1/r$  where  $r$  is the distance between the black hole and the observer. As  $d \ll r$ , this condition is easily satisfied. For  $\omega d \gg 1$  (geometric optics limit), we obtain

$$\Phi_{\text{I}}(\vec{X}_{\text{I}}) \propto \delta^2 \left( \vec{X}_{\text{I}} + f S'' \vec{X}_* \right). \quad (20)$$

Thus we recover a point image of the point source on the image plane; the location of the image corresponds to the location determined by the null geodesics. If we do not take geometric optics limit, the image acquires diffraction effects and the image of the point source has a fine size called the Airy disk. We apply this model of image formation to scattering problems by black holes and obtain images of black holes (Fig. 1). For a point  $(X, Y)$  on the lens plane  $Z = 0$ , the angle between this point and the  $\bar{z}$  axis is given by

$$\cos \theta = \frac{X}{r} \sin \theta_0 + \sqrt{1 - \left( \frac{X}{r} \right)^2 - \left( \frac{Y}{r} \right)^2} \cos \theta_0. \quad (21)$$

We use this relation to evaluate the Fourier integral (17) to obtain images.

As an example of image reconstruction from scattering waves, we present the gravitational lensing by a point source. Assuming that the gravitational field is weak, the wave equation for the massless scalar field reduces to the Newtonian form [4]

$$\nabla^2 \Phi_N + \left( \omega^2 + \frac{4M\omega^2}{r} \right) \Phi_N = 0, \quad (22)$$

where  $\nabla^2$  is the flat space Laplacian and the problem is equivalent to that of the Coulomb scattering in quantum mechanics. The exact wave function for the scattering problem with a plane wave incident from infinity is given by

$$\Phi_N(\theta_0) = e^{\pi\omega M} \Gamma(1 - 2i\omega M) e^{i\omega r \cos \theta_0} {}_1F_1(2i\omega M, 1; i\omega r(1 - \cos \theta_0)). \quad (23)$$

The wave amplitude at  $r = 20M$  is shown in Fig. 3. For small scattering angle, oscillatory behavior due to diffraction between the incident wave and the scattered wave can be observed. The behavior of the scattering amplitude for small scattering angle (forward direction) can be obtained by the asymptotic behavior of the confluent geometric function:

$$\Phi_N(\theta_0) \propto J_0(2\omega\sqrt{Mr}\theta_0) \quad \text{for } |\theta_0| \ll 1. \quad (24)$$

The Fourier transformation (17) for this function results in the function with a peak at the angular radius  $\theta_E \equiv \sqrt{4M/r}$ , that corresponds to the Einstein ring. On the other hand, for large value of  $\theta_0$ , the diffraction effect becomes small and a ring image does not appear in the backward direction.

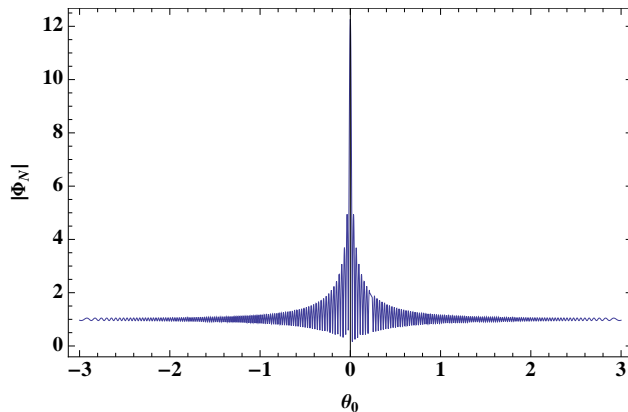


FIG. 3: The wave amplitude  $|\Phi_N|$  for  $M\omega = 12$  at  $r = 20M$ .

The reconstructed images from the scattering wave using (17) are shown in Fig. 4. For  $\theta_0 = 0$ , we obtain an image of the Einstein ring with angular radius  $\theta_E$ . For  $\theta_0 \neq 0$ , double images of the point source appear. These results reproduce images of the gravitational lensing obtained by the ray tracing method using the lens equation.

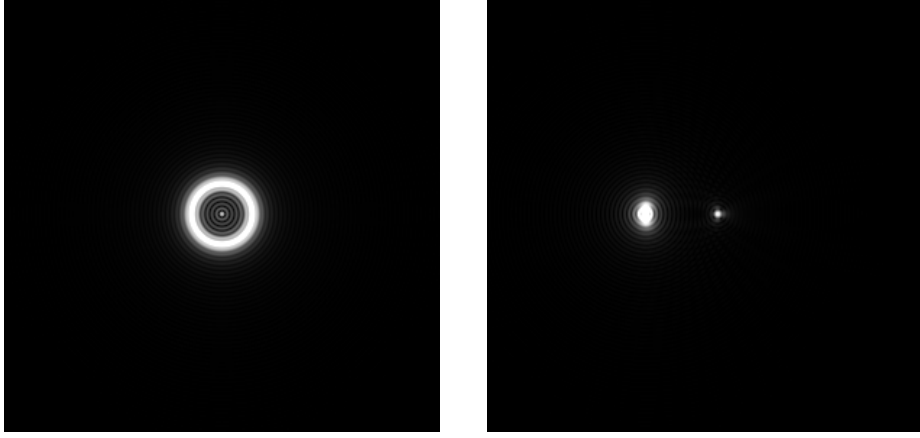


FIG. 4: The left panel is the image for  $\theta_0 = 0$  and this is the Einstein ring. The angular radius of the ring is given by  $\theta_E$ . The right panel is the image for  $\theta_0 = \pi/4$  and double images of the source appear. These images are obtained for  $\omega M = 12, r = 20M, d/r = 0.2$ .

#### IV. NUMERICAL RESULTS OF WAVE SCATTERING BY BLACK HOLE

We numerically solved the massless field in the Schwarzschild spacetime for the angular frequencies  $M\omega = 2, 12, 24$  and the source positions  $r_S = 2.5M, 3M, 6M, 15M$ . The detector is located at  $r_{\text{obs}} = 20M$ . The numerical grid size is  $1001 \times 1001$ . We have also done the calculation with the grid size  $501 \times 501$  to check the validity of our numerical results. In this paper, we only present the result for  $M\omega = 2, 12$  and  $r_S = 2.5M, 6M$ .

##### A. $M\omega = 12$ case

We first present the result for  $M\omega = 12$  case. The source position is  $r_S = 6M$  and moderately far from the black hole. This setting corresponds to the standard analysis of wave scattering by black holes that the source is placed at spatial infinity and the incident wave is treated as a plane wave. At the location of the observer, we do not distinguish the incident waves and the scattered waves. Hence the detector receives both the incident waves and the scattering waves, and their superposed wave amplitude is obtained. As the result, despite of the long range Coulomb like nature of the gravitational field, “scattering amplitude”  $|\Phi_{\text{obs}}|$  remains finite even for small scattering angles (see Fig. 6). The situation is the same as the gravitational lensing presented in the last section. The standard handling of the scattering problem extracts purely scattered wave and results in diverging scattering amplitude for small scattering angle (forward direction) due to the long range nature of the gravitational force.

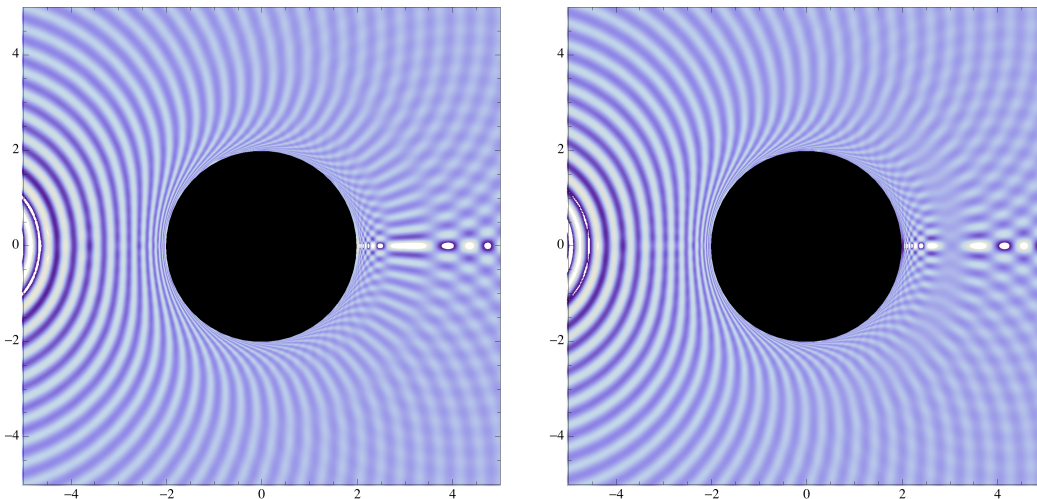


FIG. 5: Spatial distribution of  $\Phi$  for  $M\omega = 12$  on  $(\bar{z}, \bar{x})$  plane. Left panel:  $\text{Re}[\Phi]$ . Right panel:  $\text{Im}[\Phi]$ . The point source is placed at  $(\bar{z}, \bar{x}) = (-6M, 0)$ .

Fig. 5 shows the distribution of  $\Phi$  on  $(\bar{z}, \bar{x})$  plane. We can observe that the wavelength of the incident wave becomes shorter near the black hole horizon due to gravitational blue shift. Along the  $\bar{z}$  axis ( $\bar{z} > 0$ ), the amplitude of the wave is enhanced due to constructive interference of scattered waves. It is also possible to observe the characteristic wave pattern formed around the unstable orbit  $r = 3M$ .

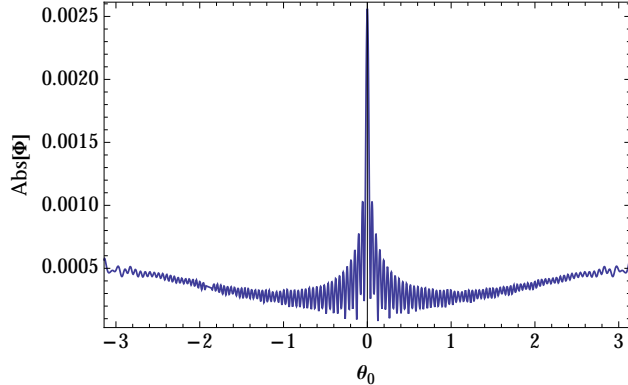


FIG. 6: The observed wave amplitude at  $r_{\text{obs}} = 20M$ .  $M\omega = 12$ ,  $r_S = 6M$ .

As already mentioned, the wave amplitude remains finite for  $\theta_0 \sim 0$ . The wave amplitude has oscillatory behavior for all values of the scattering angle. This is contrasted with the scattering amplitude for the gravitational lensing. Except for  $\theta_0 \sim 0$ , the wave amplitude increases as the scattering angle increases. As the distance from the point source to the observer varies depending on the scattering angle, the observed wave amplitude increases for the backward direction because the distance between the source and the observer decreases. The oscillatory behavior of the wave amplitude at the forward and the backward directions corresponds to so called glory effect [3, 5] and it is possible to identify the glory in images in our analysis. For black holes, glories arise because a wave can be deflected through an angle greater than  $\pi$  and the glory scattering is associated with the unstable photon orbit at  $r = 3M$ .

The reconstructed images from the scattering wave are shown in Fig. 7. We have applied the formula (17) with  $d/r_{\text{obs}} = 0.5$  to obtain these images. For  $\theta_0 = 0$ , the image is a ring that corresponds to the forward glory. As is known, the scattering amplitude for the forward and the backward glory is given by [3, 5]

$$\Phi(\theta_0) \sim J_0(\ell_g \theta_0) \quad (25)$$

where  $\ell_g = 3\sqrt{3}M\omega$  corresponds to the critical impact parameter that the incident null ray can escape to infinity. In terms of images obtained by the Fourier transformation of (25), the apparent angular radius of the ring is given by

$$\theta_g = \frac{3\sqrt{3}M}{r}. \quad (26)$$

The solution (25) and the relation (26) can be used to check the numerical result. For the backward direction  $\theta_0 = \pi$ , we cannot identify the ring image well because it is drown in the wave of the point source. But in the plot of the intensity distribution (Fig. 8), we can identify small dips of the intensity at the radius corresponding to the ring of the backward glory.



FIG. 7: Images of black holes reconstructed from scattering waves ( $M\omega = 12, r_S = 6M$ ). From the top left panel to the bottom right panel, the scattering angles are  $\theta_0 = 0, \pi/4, \pi/2, 3\pi/4, \pi$ .

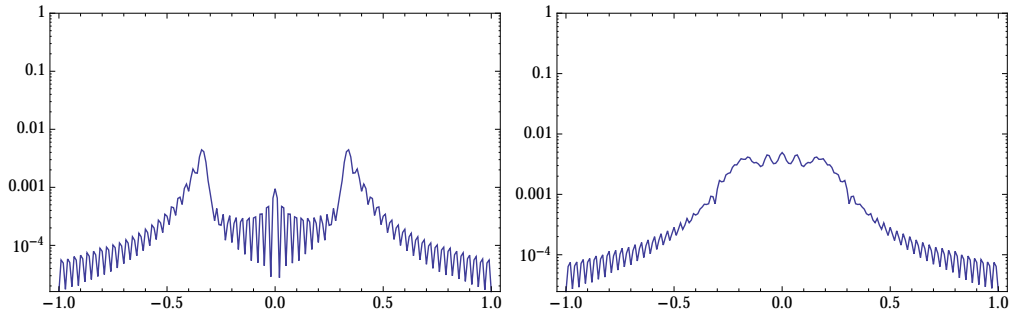


FIG. 8: The intensity distribution of images. Left panel:  $\theta_0 = 0$  (forward). Right panel:  $\theta_0 = \pi$  (backward).

In the geometric optics limit, images of black holes can be obtained by solving null geodesics. For the observer at  $\theta_0 = 0$ , the primary null rays, which are deflected by the black hole but do not go around it, result in the Einstein ring. The secondary and the higher degrees of null rays that go around the black hole many times also form ring images with smaller angular radius compared to the Einstein ring. The left panel in Fig. 9 shows an example of the primary and the secondary null rays connecting the source and the observer at  $\theta_0 = 0$ . The right panel in Fig. 9 shows the apparent angular radius of the Einstein ring and the ring by the secondary rays as the function of the source position  $r_S$ . For  $r_S = 6M$ , the ratio of angular sizes of these two rings are  $\sim 1.2$ .



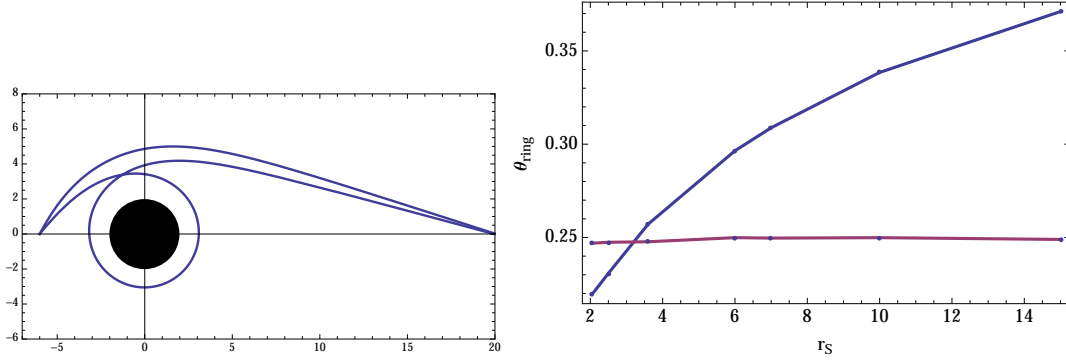


FIG. 9: Left panel: the primary and the secondary null rays connecting the source at  $r_S = 6M$  and the observer at  $r_{\text{obs}} = 20M$ . These rays constitute ring images. Right panel: The apparent angular radius of ring images for different location of the source. The blue line corresponds to the primary rays (Einstein ring) and the red line corresponds to the secondary rays.

We expect to observe these double ring structure in our image reconstructed from the scattering waves. However, as are shown in Fig. 7 and Fig. 8, it is not possible to identify this structure because it is buried in the diffraction pattern appeared in the image. We cannot conclude the observed second diffraction peak in Fig. 8 really corresponds to the Einstein ring. By using higher frequency waves, identification of the double ring structure of the images will be succeed. For this purpose, we present the image using the wave with  $M\omega = 24$  (Fig. 10). The highest peak of the intensity corresponds to the unstable orbit and it is possible to observe a broad second peak outside of it. The measured radius of the second peak is about 1.2 times larger than that of the unstable orbit and we can conclude that the second peak corresponds to the Einstein ring.

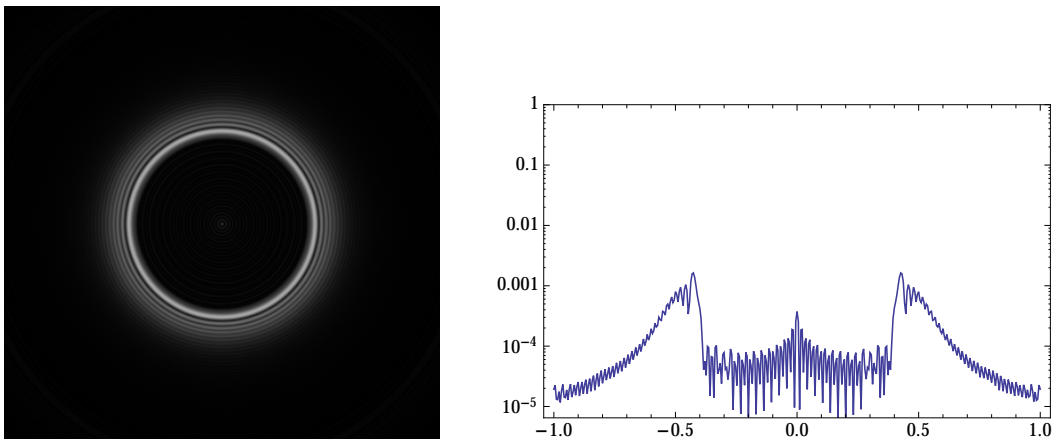


FIG. 10: Left panel: image for  $\theta_0 = 0$  using the wave with  $M\omega = 24, d/r_{\text{obs}} = 0.6$ . Right panel: intensity distribution of the image.

We then consider the case that the source is near the black hole  $r_S = 2.5M$ ; in this case, the source is placed inside the unstable orbit  $3M$ . We do not observe significant difference of the scattering behavior of waves compared to  $r_S = 6M$  case (Figs. 11 and 12).

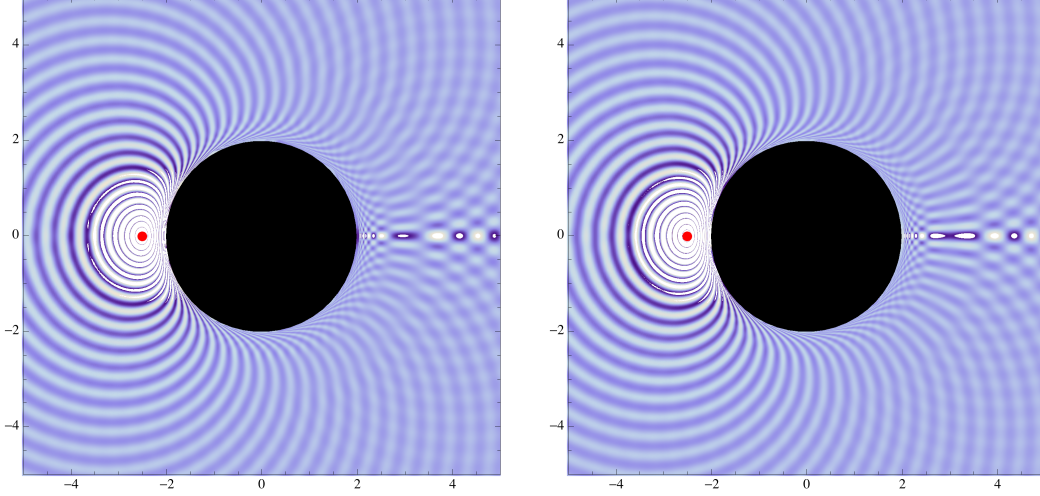


FIG. 11: Spatial distribution of  $\Phi$  on  $(\bar{z}, \bar{x})$  plane for  $M\omega = 12$ . Left panel:  $\text{Re}[\Phi]$ . Right panel:  $\text{Im}[\Phi]$ . The point source is located at  $(\bar{z}, \bar{x}) = (-2.5M, 0)$ .

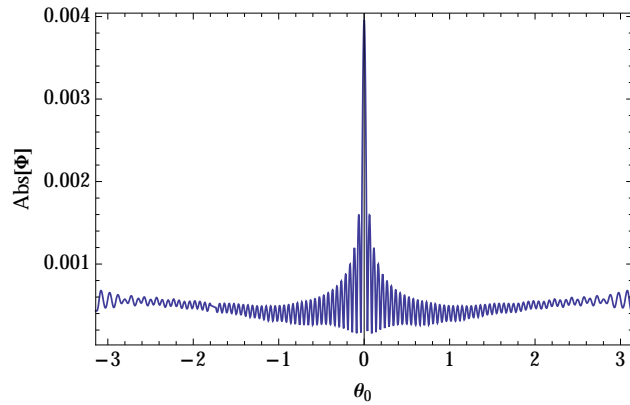


FIG. 12: The scattering amplitude at  $r_{\text{obs}} = 20M$ .  $M\omega = 12, r_S = 2.5M$ .

In this case, it is possible to observe a ring for the backward direction  $\theta_0 = \pi$  in image (Figs. 13 and 14) because the distance between the source and the observer is larger than  $r_S = 6M$  case and the amplitude of the wave that directly reaches the observer reduces. This enables us to observe the backward glory as a ring image.

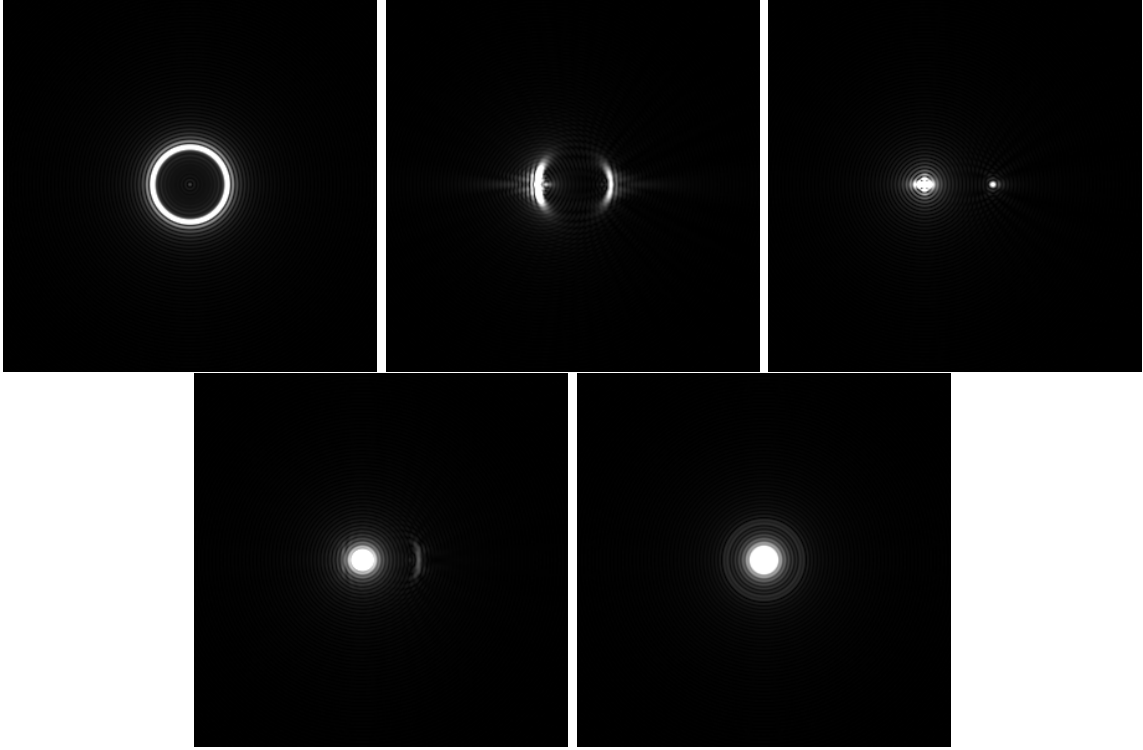


FIG. 13: Images of black holes reconstructed from scattering waves. From the top left panel to the bottom right panel, the scattering angles are  $\theta_0 = 0, \pi/4, \pi/2, 3\pi/4, \pi$ .

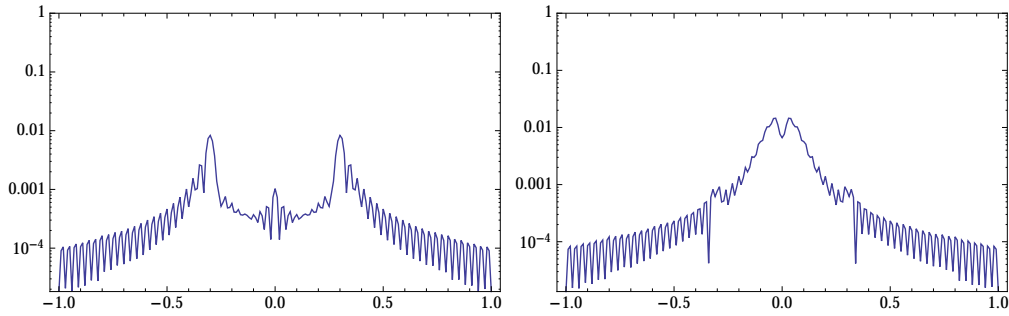


FIG. 14: The intensity distribution of images. Left panel:  $\theta_0 = 0$ . Right panel:  $\theta_0 = \pi$ .

### B. $M\omega = 2$ case

The wavelength of the source field longer than  $M\omega = 12$  case and the wave effects become more significant. Fig. 15 shows spatial distribution of waves around the black hole. The source position is  $r_S = 6M$ .

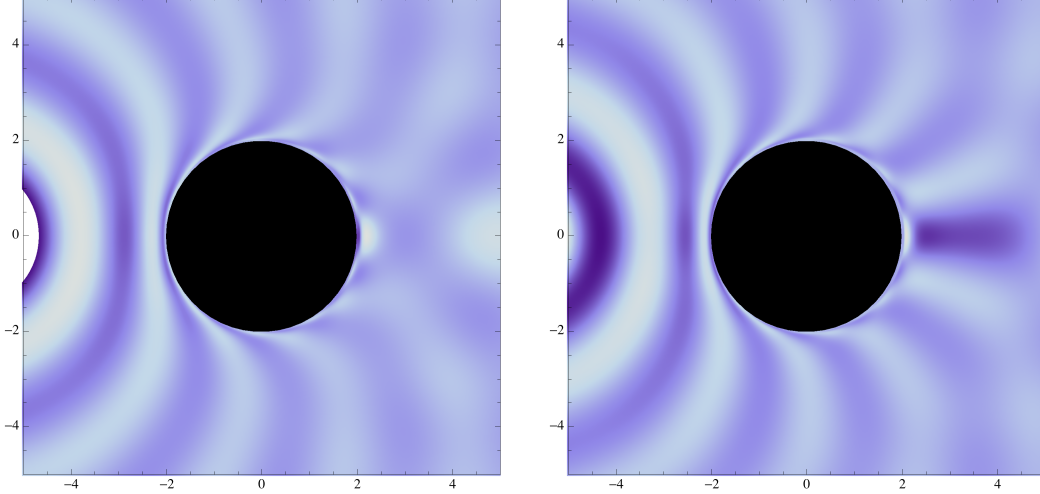


FIG. 15: Spatial distribution of  $\Phi$  on  $(\bar{z}, \bar{x})$  plane for  $M\omega = 2$ . Left panel:  $\text{Re}[\Phi]$ . Right panel:  $\text{Im}[\Phi]$ . The point source is located at  $(\bar{z}, \bar{x}) = (-6M, 0)$ .

The scattering amplitude also shows interference pattern (Fig. 16). The distance between adjacent fringes becomes larger compared to  $M\omega = 12$  case. But the characteristic feature is the same.

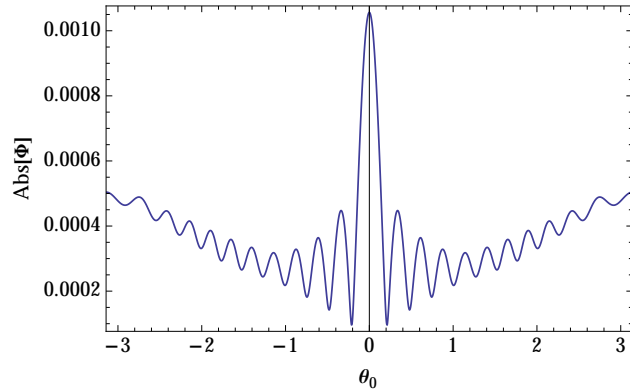


FIG. 16: The scattering amplitude at  $r_{\text{obs}} = 20M$ .  $M\omega = 2, r_S = 6M$ .

In this case, we can also observe a ring image for  $\theta_0 = 0$  corresponding to the unstable orbit (Figs. 17 and 18).

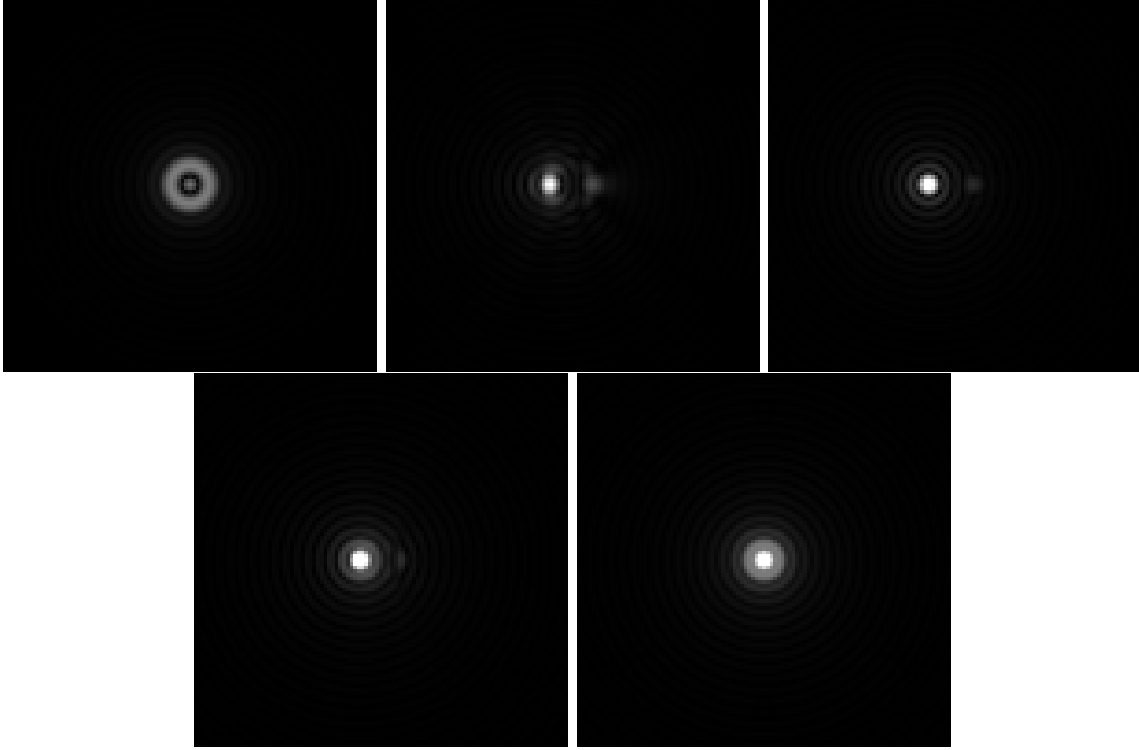


FIG. 17: Images of black holes reconstructed from scattering waves. From the top left panel to the bottom right panel, the scattering angles are  $\theta_0 = 0, \pi/4, \pi/2, 3\pi/4, \pi$ .

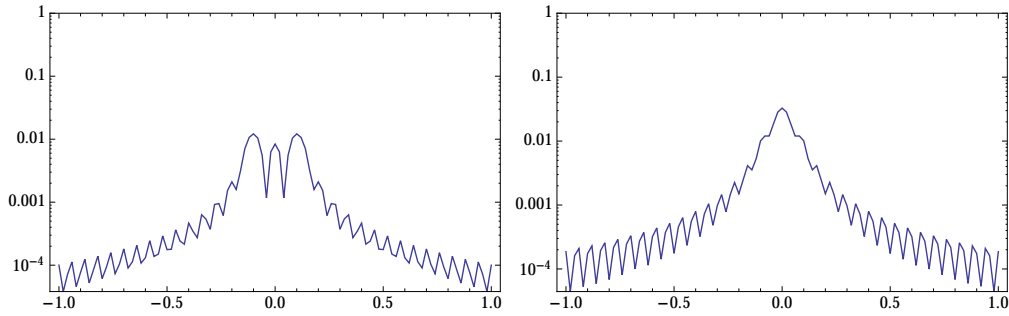


FIG. 18: The intensity distribution of images. Left panel:  $\theta_0 = 0$ . Right panel:  $\theta_0 = \pi$ .

Finally, we present the result for the source position  $r_S = 2.5M$  (Figs. 19 and 20). In this case, we can identify both the forward and the backward glories as ring images (Figs. 21 and 22).

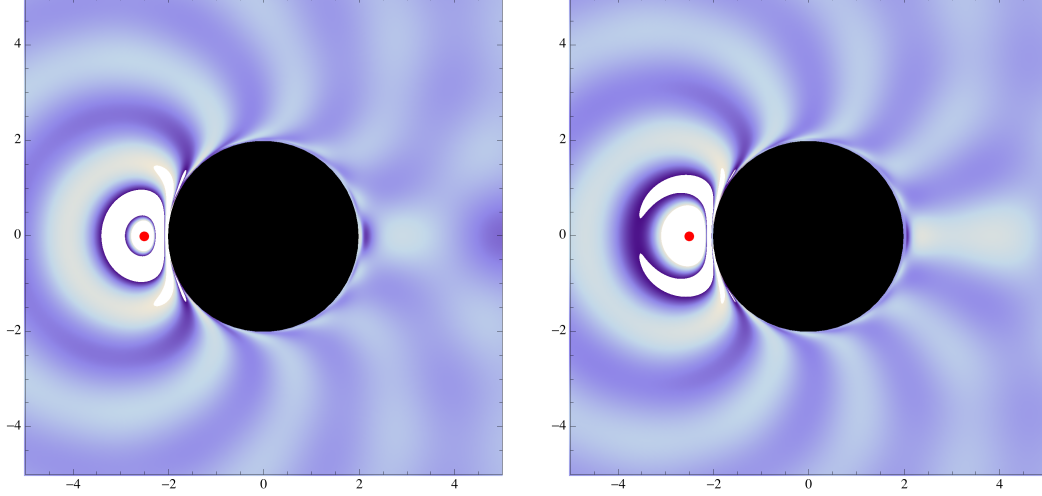


FIG. 19: Spatial distribution of  $\Phi$  on  $(\bar{z}, \bar{x})$  plane for  $M\omega = 2$ . Left panel:  $\text{Re}[\Phi]$ . Right panel:  $\text{Im}[\Phi]$ . The point source is located at  $(\bar{z}, \bar{x}) = (-2.5M, 0)$ .

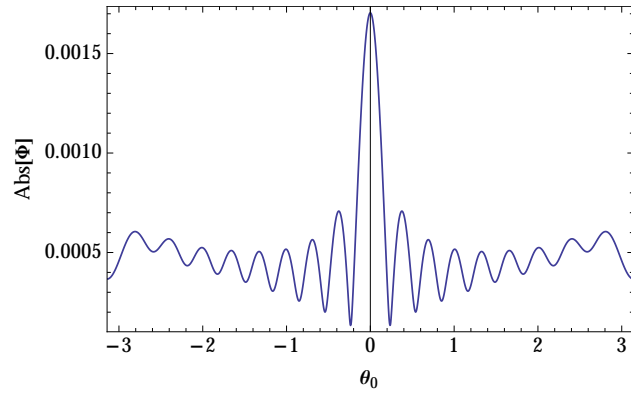


FIG. 20: The scattering amplitude at  $r_{\text{obs}} = 20M$ .  $M\omega = 2$ ,  $r_S = 2.5M$ .

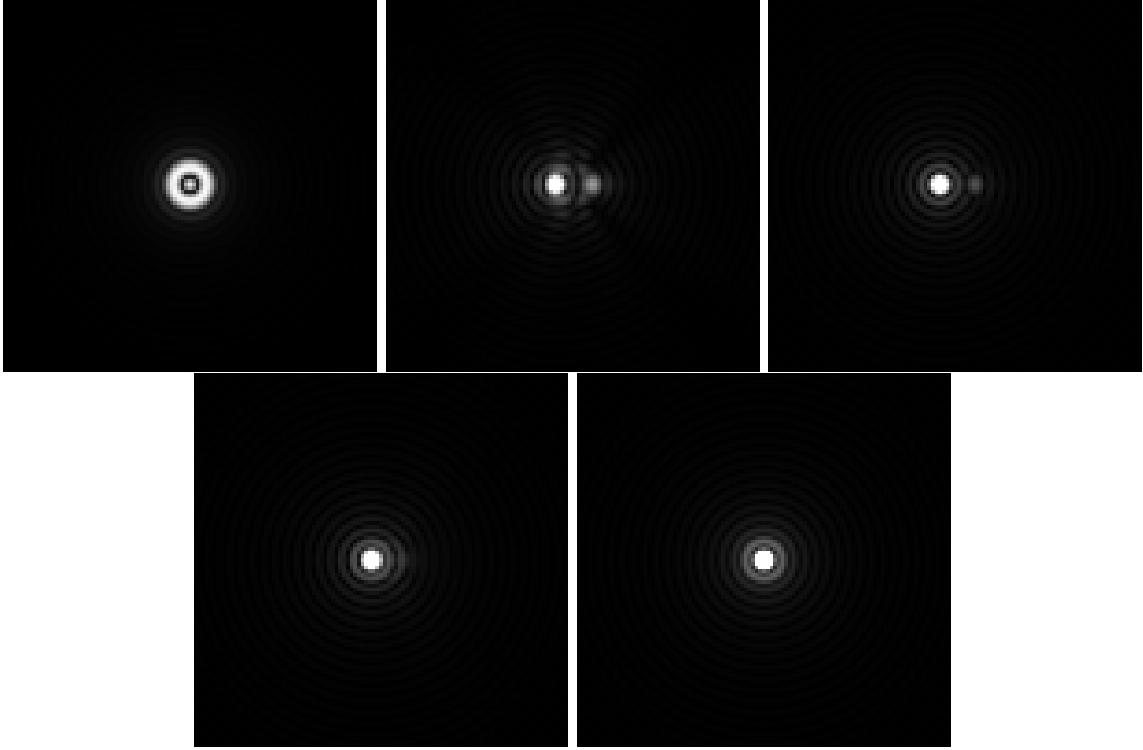


FIG. 21: Images of black holes reconstructed from scattering waves. From the top left to the bottom right panel, the scattering angles are  $\theta_0 = 0, \pi/4, \pi/2, 3\pi/4, \pi$ .

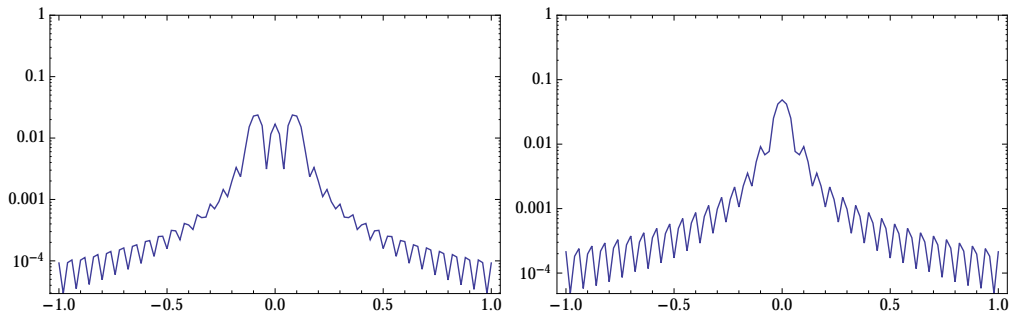


FIG. 22: The intensity distribution of images. Left panel:  $\theta_0 = 0$ . Right panel:  $\theta_0 = \pi$ .

## V. SUMMARY AND DISCUSSION

We investigated scattering of scalar waves by the Schwarzschild black hole. Our main aim of this analysis is to obtain images of black holes using waves. For this purpose, we solved the scalar wave equation in the Schwarzschild spacetime numerically and reconstructed images of black holes by the Fourier transformation of the scattering waves. For the forward and the backward direction of the scattering, we obtained ring images corresponding to the glory scattering by the black hole. In the geometric optics limit, these ring images are related to existence of the unstable orbit for null rays. As extension of analysis presented in this paper, wave scattering and image formation in the Kerr geometry is an interesting subject

to be tackled. For the Kerr black hole, due to dragging of the spacetime, incident waves can be amplified by the superradiance [10]. By investigating images from scattered waves by the Kerr black hole, we expect to find out a new aspect and an interpretation of the superradiance in connection with the Penrose process. We will report on the analysis of the Kerr black hole case in our next publication.

Another application of the analysis presented in this paper is related to observations of black hole shadows [14, 15]. As the apparent angular sizes of black hole shadows are so small, the diffraction effect on images are crucial to resolve black hole shadows in observation using radio interferometer. For SgrA\*, which is the black hole candidate at Galactic center, the apparent angular size of its shadow is estimated to be  $\sim 30\mu$  arcsec and this value is the largest among black hole candidates. The resolving power of the image formation system is given by [13]

$$\theta_0 = \frac{\lambda}{D}, \quad (27)$$

where  $\lambda$  is the wave length and  $D$  is the size of “lens”. For the radio interferometer,  $D$  corresponds to the baseline length between antennas. For a sub-mm VLBI,  $\lambda \sim 0.1\text{mm}$  and the condition  $\theta_0 < 30\mu$  arcsec yields  $D > 1000\text{km}$ . This requirement for the baseline length shows the possibility of detecting the black hole shadow of SgrA\* using the present day technology of VLBI telescope. Thus, analysis of black hole shadows based on wave optics is an important theme for successful detection of shadows and determination of black hole parameters via imaging of black holes.

### Acknowledgments

This work was supported in part by the JSPS Grant-In-Aid for Scientific Research (C) (23540297). The authors thank all member of “black hole horizon project meeting” in which the preliminary version of this paper was presented.

- 
- [1] H. M. Nussenzveig, *Diffraction Effects in Semiclassical Scattering* (Cambridge University Press, 1992).
  - [2] T. Regge and J. A. Wheeler, *Phys. Rev.* **108**, (1957) 1063.
  - [3] R. A. Matzner, C. DeWitte-Moretter, B. Nelson, and T.-R. Zhang, “Glory scattering by black holes”, *Phys. Rev. D* **31**, (1985) 1869–1878.
  - [4] J. A. H. Futterman, F. A. Handler, and R. A. Matzner, *Scattering from black holes* (Cambridge Univ. Press, 1988).
  - [5] P. Anninos, C. DeWitt-Morette, R. A. Matzner, P. Yioutas, and T. R. Zhang, “Orbiting cross sections: Application to black hole scattering”, *Phys. Rev. D* **46**, (1992) 4477–4494.
  - [6] N. Anderson, “Scattering of massless scalar waves by a Schwarzschild black holes: A phase-integral study”, *Phys. Rev. D* **52**, (1995) 1808–1820.
  - [7] N. Anderson and B. Jensen, “Scattering by Black Holes”, *arXiv:gr-qc/0011025* .
  - [8] K. Glampedakis and N. Anderson, “Scattering of scalar waves by rotating black holes”, *Class. Quantum Grav.* **18**, (2001) 1939–1966.
  - [9] S. R. Dolan, “Scattering and absorption of gravitational waves by rotating black holes”, *Class. Quantum Grav.* **25**, (2008) 235002.



- [10] V. P. Frolov and I. D. Novikov, *Black Hole Physics* (Kluwer Academic Publishers, 1998).
- [11] Y. Nambu, “Wave optics and image formation in gravitational lensing”, *Journal of Physics Conference Series* **410**, (2013) 012036.
- [12] Y. Nambu, “Wave optics and image formation in gravitational lensing”, *Int. J. Astro. Astrophys.* **3**, (2013) 1–7, arXiv:1207.6846.
- [13] K. K. Sharma, *Optics: principles and applications* (Academic Press, 2006).
- [14] H. Falcke, F. Melia, and E. Agol, “Viewing the shadow of the black hole at the galactic center”, *Astrophys. J.* **528**, (2000) L13–L16.
- [15] M. Miyoshi, K. Ishitaska, S. Kamenno, and Z.-Q. Shen, “Direct imaging of the black hole, SgrA\*”, *Prog. Theor. Phys. Suppl.* **155**, (2004) 186–189.

### Appendix: finite difference method

To solve the Helmholtz equation (4) numerically, we should rewrite the equation into the corresponding difference equation. For our numerical calculation, we divide the considering spatial region in  $(x, \theta)$  space into  $(N + 1) \times (N + 1)$  homogeneous grids. The coordinate variables are

$$x_i = x_0 + i \cdot \Delta, \quad \theta_j = j \cdot \Delta_\theta, \quad i, j = 0, \dots, N, \quad (\text{A.1})$$

where  $\Delta$  and  $\Delta_\theta$  are the spacing of the grids in  $x$  and  $\theta$  coordinates, respectively. The coordinates range of the numerical box is

$$x_0 \leq x \leq x_0 + N\Delta, \quad 0 \leq \theta \leq N\Delta_\theta \equiv \pi. \quad (\text{A.2})$$

Accordingly, the field  $\hat{\Phi}$  at the point  $(x_i, \theta_j)$  is written as  $\hat{\Phi}_{i,j} \equiv \hat{\Phi}(x_i, \theta_j)$ . Then, Eq. (4) in the finite difference form is given by

$$\begin{aligned} & \frac{\hat{\Phi}_{i+1,j} + \hat{\Phi}_{i-1,j} - 2\hat{\Phi}_{i,j}}{\Delta^2} + \frac{1}{r_i^2} \left(1 - \frac{2}{r_i}\right) \left( \cot \theta_j \frac{\hat{\Phi}_{i,j+1} - \hat{\Phi}_{i,j-1}}{2\delta\Delta} + \frac{\hat{\Phi}_{i,j+1} + \hat{\Phi}_{i,j-1} - 2\hat{\Phi}_{i,j}}{\delta^2\Delta^2} \right) \\ & + \left[ M^2\omega^2 - \frac{2}{r_i^3} \left(1 - \frac{2}{r_i}\right) \right] \hat{\Phi}_{i,j} = S_{i,j} \end{aligned} \quad (\text{A.3})$$

and Eq. (12) is rewritten as

$$\begin{aligned} & \frac{\hat{\Phi}_{i+1,j} + \hat{\Phi}_{i-1,j} - 2\hat{\Phi}_{i,j}}{\Delta^2} + \frac{2}{r_i^2} \left(1 - \frac{2}{r_i}\right) \frac{\hat{\Phi}_{i,j+1} + \hat{\Phi}_{i,j-1} - 2\hat{\Phi}_{i,j}}{\delta^2\Delta^2} \\ & + \left[ M^2\omega^2 - \frac{2}{r_i^3} \left(1 - \frac{2}{r_i}\right) \right] \hat{\Phi}_{i,j} = S_{i,j} \end{aligned} \quad (\text{A.4})$$

where we have introduced  $\delta = \Delta_\theta/\Delta$  and  $r_i$  is defined as  $r_i = r(x_i)$ . In these equations, the radial coordinate is measured in the unit of the black hole mass  $M$ .

The boundary conditions for the  $r$  direction of the Helmholtz equation must be imposed using Eq. (7) and Eq. (8) to determine  $\hat{\Phi}_{-1,j}$  and  $\hat{\Phi}_{N+1,j}$ . These equations are conditions for temporal behavior of waves. Thus we have to translate these conditions for the wave field to that does not contain the time dependence. We first consider Eq. (7). This equation relates the wave field at the inner spatial boundary  $x_0$  and  $x_{-1}$ . As the solution of this equation is  $\hat{\Phi}(t, x) = \hat{\Phi}(t + x)$ , the field value  $\hat{\Phi}(t + \Delta_t, x_{-1})$  is expressed as

$$\hat{\Phi}(t + \Delta_t, x_{-1}) = \hat{\Phi}(t, x_{-1} + \Delta_t). \quad (\text{A.5})$$

As the time dependence of the wave is assumed to be  $\hat{\Phi}(t) \propto e^{-iM\omega t}$ , this boundary condition (7) provides the following relation between the field values at  $x_0$  and  $x_{-1}$ :

$$e^{iM\omega\Delta_t}\hat{\Phi}_{-1,j} = \hat{\Phi}_{-1,j} + \frac{\Delta_t}{\Delta}(\hat{\Phi}_{0,j} - \hat{\Phi}_{-1,j}). \quad (\text{A.6})$$

Thus,  $\hat{\Phi}_{-1,j}$  can be determined by

$$\hat{\Phi}_{-1,j} = \frac{-\delta_t}{1 - \delta_t - e^{-iM\omega\delta_t\Delta}}\hat{\Phi}_{0,j} \quad (\text{A.7})$$

where  $\delta_t \equiv \Delta_t/\Delta$ . The boundary condition at the outer spatial boundary can be obtained in the similar way and we have

$$\hat{\Phi}_{N+1,j} = \frac{-\delta_t}{1 - \delta_t - e^{-iM\omega\delta_t\Delta}}\hat{\Phi}_{N,j}. \quad (\text{A.8})$$

In our numerical analysis, we set  $\delta_t = 1$  and we adopt the following equations to impose the boundary conditions at the inner and the outer spatial boundaries:

$$\hat{\Phi}_{-1,j} = e^{iM\omega\Delta}\hat{\Phi}_{0,j}, \quad \hat{\Phi}_{N+1,j} = e^{iM\omega\Delta}\hat{\Phi}_{N,j}. \quad (\text{A.9})$$

The boundary conditions on the  $\bar{z}$  axis are determined by Eq. (9) and

$$\hat{\Phi}_{i,-1} = \hat{\Phi}_{i,1}, \quad \hat{\Phi}_{i,N+1} = \hat{\Phi}_{i,N-1}. \quad (\text{A.10})$$

In the numerical grid space, the location of the point source is  $(x_{i_S}, \pi)$ . Equation (13) yields field values at points  $(x_{i_S-1}, \pi)$ ,  $(x_{i_S+1}, \pi)$  and  $(x_{i_S}, \pi - \Delta_\theta)$ :

$$\hat{\Phi}_{i_S-1,N} = \hat{\Phi}_{i_S+1,N} = \frac{Ar_S e^{i\omega\Delta}}{\Delta\sqrt{1-2M/r_S}}, \quad \hat{\Phi}_{i_S,N-1} = \frac{A}{\Delta_\theta} e^{i\omega r_S \Delta_\theta / \sqrt{1-2M/r_S}}. \quad (\text{A.11})$$

(A.11) provides the boundary condition for the wave equation around the point source.

These difference equations and the boundary conditions constitute the simultaneous equations. The simultaneous equations are written in a matrix form as

$$\mathbf{A} \cdot \mathbf{x} = \mathbf{b} \quad (\text{A.12})$$

where  $\mathbf{x}$  is the vector to be solved and the matrix  $\mathbf{A}$  and the vector  $\mathbf{b}$  are determined by the difference equation. As demonstrations, let us first consider the  $3 \times 3$  grids case. The components of  $\mathbf{A}$ ,  $\mathbf{x}$  and  $\mathbf{b}$  are

$$\mathbf{A} = \begin{pmatrix} \mathbf{C}_1 & \mathbf{D}_1 & \mathbf{0} \\ \mathbf{H}_1 & \mathbf{C}_2 & \mathbf{H}_1 \\ \mathbf{0} & \mathbf{D}_1 & \mathbf{C}_1 \end{pmatrix}, \quad \mathbf{x} = \begin{pmatrix} \hat{\Phi}_{0,0}^R \\ \hat{\Phi}_{0,0}^I \\ \hat{\Phi}_{1,0}^R \\ \hat{\Phi}_{1,0}^I \\ \vdots \\ \hat{\Phi}_{2,2}^R \\ \hat{\Phi}_{2,2}^I \end{pmatrix}, \quad \mathbf{b} = \begin{pmatrix} S_{0,0}^R \\ S_{0,0}^I \\ S_{1,0}^R \\ S_{1,0}^I \\ \vdots \\ S_{2,2}^R \\ S_{2,2}^I \end{pmatrix}, \quad (\text{A.13})$$

where  $\hat{\Phi}^R$  and  $\hat{\Phi}^I$  represent the real and the imaginary part of  $\hat{\Phi}$ , respectively.  $\mathbf{C}_1, \mathbf{C}_2, \mathbf{D}_1$  and  $\mathbf{H}_1$  are  $6 \times 6$  matrices given by

$$\mathbf{C}_1 = \begin{pmatrix} c_0 & -a_0 & r_0^4 \delta^2 & 0 & 0 & 0 \\ a_0 & c_0 & 0 & r_0^4 \delta^2 & 0 & 0 \\ r_1^4 \delta^2 & 0 & d_1 & 0 & r_1^4 \delta^2 & 0 \\ 0 & r_1^4 \delta^2 & 0 & d_1 & 0 & r_1^4 \delta^2 \\ 0 & 0 & r_2^4 \delta^2 & 0 & c_2 & -a_2 \\ 0 & 0 & 0 & r_2^4 \delta^2 & a_2 & c_2 \end{pmatrix}, \quad (\text{A.14})$$

$$\begin{aligned} a_i &= r_i^4 \delta^2 \sin(M\omega\Delta), \\ c_i &= \delta^2 \Delta^2 (M^2 \omega^2 r_i^4 - 2(r_i - 2)) - 2r_i^4 \delta^2 - 4r_i(r_i - 2) + r_i \delta^2 \cos(M\omega\Delta), \\ d_i &= \delta^2 \Delta^2 (M^2 \omega^2 r_i^4 - 2(r_i - 2)) - 2r_i^4 \delta^2 - 4r_i(r_i - 2), \end{aligned}$$

$$\mathbf{C}_2 = \begin{pmatrix} h_0 & -2a_0 & 2r_0^4 \delta^2 & 0 & 0 & 0 \\ 2a_0 & h_0 & 0 & 2r_0^4 \delta^2 & 0 & 0 \\ 2r_1^4 \delta^2 & 0 & k_1 & 0 & 2r_1^4 \delta^2 & 0 \\ 0 & 2r_1^4 \delta^2 & 0 & k_1 & 0 & 2r_1^4 \delta^2 \\ 0 & 0 & 2r_2^4 \delta^2 & 0 & h_2 & -2a_2 \\ 0 & 0 & 0 & 2r_2^4 \delta^2 & 2a_2 & h_2 \end{pmatrix}, \quad (\text{A.15})$$

$$\begin{aligned} h_i &= 2\delta^2 \Delta^2 (M^2 \omega^2 r_i^4 - 2(r_i - 2)) - 4r_i^4 \delta^2 - 4r_i(r_i - 2) + 2r_i \delta^2 \cos(M\omega\Delta), \\ k_i &= 2\delta^2 \Delta^2 (M^2 \omega^2 r_i^4 - 2(r_i - 2)) - 4r_i^4 \delta^2 - 4r_i(r_i - 2), \end{aligned}$$

$$\mathbf{D}_1 = \text{diag} \left[ 4r_0(r_0 - 2), 4r_0(r_0 - 2), 4r_1(r_1 - 2), 4r_1(r_1 - 2), 4r_2(r_2 - 2), 4r_2(r_2 - 2) \right], \quad (\text{A.16})$$

$$\begin{aligned} \mathbf{H}_j &= \text{diag} \left[ r_0(r_0 - 2)(2 - \delta\Delta \cot \theta_j), r_0(r_0 - 2)(2 - \delta\Delta \cot \theta_j), r_1(r_1 - 2)(2 - \delta\Delta \cot \theta_j), \right. \\ &\quad \left. r_1(r_1 - 2)(2 - \delta\Delta \cot \theta_j), r_2(r_2 - 2)(2 - \delta\Delta \cot \theta_j), r_2(r_2 - 2)(2 - \delta\Delta \cot \theta_j) \right]. \end{aligned} \quad (\text{A.17})$$

In the case of  $4 \times 4$  grids, the structure of  $\mathbf{x}$  and  $\mathbf{A}$  becomes as follows:

$$\mathbf{x} = \begin{pmatrix} \hat{\Phi}_{0,0}^R \\ \hat{\Phi}_{0,0}^I \\ \hat{\Phi}_{1,0}^R \\ \hat{\Phi}_{1,0}^I \\ \vdots \\ \hat{\Phi}_{3,3}^R \\ \hat{\Phi}_{3,3}^I \end{pmatrix}, \quad \mathbf{A} = \begin{pmatrix} \mathbf{C}_1 & \mathbf{D}_1 & \mathbf{0} & \mathbf{0} \\ \mathbf{H}_1 & \mathbf{C}_2 & \mathbf{H}_1 & \mathbf{0} \\ \mathbf{0} & \mathbf{H}_2 & \mathbf{C}_2 & \mathbf{H}_2 \\ \mathbf{0} & \mathbf{0} & \mathbf{D}_1 & \mathbf{C}_1 \end{pmatrix}. \quad (\text{A.18})$$

$\mathbf{C}_{1,2}$ ,  $\mathbf{D}_1$  and  $\mathbf{H}_{1,2}$  are  $8 \times 8$  matrices given by

$$\mathbf{C}_1 = \begin{pmatrix} c_0 & -a_0 & r_0^4 \delta^2 & 0 & 0 & 0 & 0 & 0 \\ a_0 & c_0 & 0 & r_0^4 \delta^2 & 0 & 0 & 0 & 0 \\ r_1^4 \delta^2 & 0 & d_1 & 0 & r_1^4 \delta^2 & 0 & 0 & 0 \\ 0 & r_1^4 \delta^2 & 0 & d_1 & 0 & r_1^4 \delta^2 & 0 & 0 \\ 0 & 0 & r_2^4 \delta^2 & 0 & d_2 & 0 & r_2^4 \delta^2 & 0 \\ 0 & 0 & 0 & r_2^4 \delta^2 & 0 & d_2 & 0 & r_2^4 \delta^2 \\ 0 & 0 & 0 & 0 & r_3^4 \delta^2 & 0 & c_3 & -a_3 \\ 0 & 0 & 0 & 0 & 0 & r_3^4 \delta^2 & a_3 & c_3 \end{pmatrix}, \quad (\text{A.19})$$

$$\mathbf{C}_2 = \begin{pmatrix} h_0 & -2a_0 & 2r_0^4 \delta^2 & 0 & 0 & 0 & 0 & 0 \\ 2a_0 & h_0 & 0 & 2r_0^4 \delta^2 & 0 & 0 & 0 & 0 \\ 2r_1^4 \delta^2 & 0 & k_1 & 0 & 2r_1^4 \delta^2 & 0 & 0 & 0 \\ 0 & 2r_1^4 \delta^2 & 0 & k_1 & 0 & 2r_1^4 \delta^2 & 0 & 0 \\ 0 & 0 & 2r_2^4 \delta^2 & 0 & k_2 & 0 & 2r_2^4 \delta^2 & 0 \\ 0 & 0 & 0 & 2r_2^4 \delta^2 & 0 & k_2 & 0 & 2r_2^4 \delta^2 \\ 0 & 0 & 0 & 0 & 2r_3^4 \delta^2 & 0 & h_3 & -2a_3 \\ 0 & 0 & 0 & 0 & 0 & 2r_3^4 \delta^2 & 2a_3 & h_3 \end{pmatrix}, \quad (\text{A.20})$$

$$\mathbf{D}_1 = \text{diag} \left[ 4r_0(r_0 - 2), 4r_0(r_0 - 2), 4r_1(r_1 - 2), 4r_1(r_1 - 2), 4r_2(r_2 - 2), 4r_2(r_2 - 2), \right. \\ \left. , 4r_3(r_3 - 2), 4r_3(r_3 - 2) \right], \quad (\text{A.21})$$

$$\mathbf{H}_j = \text{diag} \left[ r_0(r_0 - 2)(2 - \delta \Delta \cot \theta_j), r_0(r_0 - 2)(2 - \delta \Delta \cot \theta_j), r_1(r_1 - 2)(2 - \delta \Delta \cot \theta_j), \right. \\ \left. r_1(r_1 - 2)(2 - \delta \Delta \cot \theta_j), r_2(r_2 - 2)(2 - \delta \Delta \cot \theta_j), r_2(r_2 - 2)(2 - \delta \Delta \cot \theta_j), \right. \\ \left. r_3(r_3 - 2)(2 - \delta \Delta \cot \theta_j), r_3(r_3 - 2)(2 - \delta \Delta \cot \theta_j) \right]. \quad (\text{A.22})$$

If the number of the grids becomes larger, it is possible to predict the structure of  $\mathbf{A}$  from these examples. Of course, we should modify the forms of  $\mathbf{A}$  and  $\mathbf{b}$  to introduce a source of waves along the method we have described in (A.11).

In our calculation, the region of the numerical box is  $-2 \leq x \leq 23$  ( $2.03 \leq r \leq 20.5$ ),  $0 \leq \theta \leq \pi$  and we divide this region into  $1001 \times 1001$  grids. We used the Mathematica to obtain the solution of the linear system (A.12).